

Slip Resistance of Ti-Based High-Temperature Shape Memory Alloys

A. Ojha¹ · H. Sehitoglu¹

© ASM International 2016

Abstract Titanium with Nb, Zr, and Ta alloying substitutions possesses high plastic slip resistance and high transformation strains upon bcc (β) to orthorhombic (α'') transformation. In the current study, we determine the critical resolved shear stress (CRSS) for slip in Ti alloyed for a wide composition range of Nb, Ta, and Zr. The CRSS is obtained with a proposed Peierls–Nabarro formalism incorporating the generalized stacking fault energy barrier profile for slip obtained from the first-principles Density Functional Theory (DFT) calculations. The CRSS for slip of the orthorhombic martensite increases from 80 to 280 MPa linearly with increasing unstable fault energy. The addition of tantalum is most effective in raising the energy barriers. We also demonstrate the composition dependence of the lattice parameters of both β and α'' crystal structures as a function of Nb, Ta, and Zr additions showing agreement with experiments. Using the lattice constants, the transformation strain is determined as high as 11 % in the [011] pole and its magnitude increases mainly with Zr addition.

Keywords Shape memory · Superelasticity · Ti–Nb–Ta · Ti–Nb–Zr · Transformation strain · Slip · Martensite

Introduction

It is now well accepted that high-temperature Ti-based alloys represent a formidable class of new shape memory alloys. The research on Ti-based shape memory alloys dates back to key works in the 1970s through the early 1980s [1–5]. These alloys can be used in biomedical applications [6, 7] in addition to exhibiting high-temperature shape memory response [8–11]. Upon alloying with Nb, Zr, and Ta, high slip resistance and high transformation strains can be achieved [8, 9, 11, 12], and improving such properties is a topic of continued scientific and engineering interest. While a number of key works listed above have emphasized experiments, less work has focused on theory and simulation. For example, the plastic slip resistance is a very important parameter in constitutive modeling [13] and to achieve good shape memory functionality and fatigue resistance. In order to minimize the plastic deformation mediated via dislocation slip, it is desirable to elevate the slip stress well above the stress required to induce martensite transformation. Experiments [9, 11, 12] on Ti alloys demonstrate considerable martensite slip resistance particularly when alloyed with Zr, Nb and Ta. In addition, the slip stress magnitudes reported from these experiments are uniaxial stress magnitudes with 0.2 % strain offset, and not the CRSS levels for slip nucleation. Hence, it is imperative to establish the composition dependence of the CRSS for slip nucleation in Ti-based alloys over a wide composition range of Zr, Nb, and Ta. Most importantly, a quantitative model has not emerged that predicts the slip resistance over a broad range of compositions. This information is crucial for the design of new alloys and is the topic of this paper.

The present work represents a significant advancement in establishing the CRSS ($\tau_{\text{critical}}^{\text{slip}}$) for martensite slip, the

✉ H. Sehitoglu
huseyin@illinois.edu

¹ Department of Mechanical Science and Engineering,
University of Illinois at Urbana-Champaign, 1206 W. Green
Street, Urbana, IL 61801, USA

lattice constants (a_0 , a , b , c), and maximum transformation strains ($\epsilon_{\text{trans}}^{\text{max}}$) of a large number of Ti-based shape memory alloys which have never been explored before. The Nb, Ta, and Zr contents for Ti alloys under current investigation range from 6.25 to 37.5 at.% exceeding over 40 different compositions. In the present paper, we point to the major differences of alloying effects of Zr, Ta, and Nb on the CRSS and the transformation strains by considering the role of each element in detail. The CRSS for martensite slip is achieved with a proposed Peierls Nabarro (PN) formalism incorporating the generalized stacking fault energy (GSFE) obtained from first-principles energy calculations (DFT). The GSFE is the energy barrier per unit area required to nucleate a slip, and will be discussed later. Similarly, we establish the lattice constants of β (disordered bcc) and B19 α' (orthorhombic) phases of these alloys noting that the superelasticity in Ti alloys is achieved by the reversible thermoelastic martensite transformation between these two phases. Hereafter, the terms B19, orthorhombic and α' are used interchangeably. In addition, we investigate the composition dependence of the Nb, Ta, and Zr on the lattice constants of both crystal phases. Consequently, we undertake lattice deformation theory (LDT) calculations to obtain the maximum transformation strains of all the alloys considered in the present analysis. The details of the LDT will be discussed later.

Although binary Ti–Nb alloys exhibit superelastic properties, the transformation strains obtained for these alloys have been limited to less than 3 % [10]. However, the maximum transformation strain of over 4.3 % was obtained for the case of Ti–22Nb–(4–6)at.%Zr [12], and the experimental results confirmed that Zr addition increases the maximum transformation strain and the martensite slip stress. Consequently, the combination of high transformation strains, plastic slip resistance, and high-temperature shape memory capability make these alloys very attractive for potential applications. Some of the compositions have been studied before, but many others are investigated in the current paper, which are very promising. Therefore, we establish the CRSS for these alloys with a wider composition range of Nb, Ta and Zr that produce both a high slip resistance and a high transformation strain. We note that that the variation of slip resistance with increase in alloying content is highly non-linear, and this necessitates an accurate model for flow stress, which we propose in this study.

The determination of the lattice parameters as a first step is not trivial because there are three lattice constants (a , b , c) for martensite, which are established for different levels of volume change by conducting multiple simulations with first-principles DFT calculations. In “[Simulation Methods](#)” and “[Lattice Constant Calculations](#)” sections, we present a

detailed methodology to obtain the lattice constants of β austenite and α' martensite phase of a group of Ti–Nb–Ta and Ti–Nb–Zr alloys using DFT calculations. In “[Slip and GSFE Curves in B19 Ti Based Alloys](#)” section, we provide discussion on obtaining the GSFE for B19 (martensite) slip nucleation and the modified PN methodology to establish the CRSS for these alloys. We provide discussion and the implications of results in “[Discussion and Implications of Results](#)” section, and finally provide a summary in “[Conclusions](#)” section.

Simulation Methods

The first-principles DFT calculations were carried out to calculate the systems total energy. We utilized the Vienna ab initio Simulations Package (VASP) with the projector augmented wave (PAW) method and the generalized gradient approximation (GGA) as implementations of DFT [14, 15]. In order to simulate a disordered β crystal, a simulator code was implemented to generate a $4 \times 4 \times 2$ supercell consisting of 64 atoms. The three atom types (Ti, Nb, and Ta/Zr) were positioned randomly within the supercell yet following the composition and the bcc crystal coordinates so that the two atomic positions do not overlap with each other. It is important to note that 64 atoms supercell was large enough to obtain the converged minimum structural energy value. This was verified with independent simulations with number of atoms ranging from 16 to 96. In addition, four independent cases representing four different random solid solution alloys were investigated to see the effect of the positions of the elements on the lattice constants and the minimum structural energies. The variation of the lattice constant and the structural energy due to random alloy positioning was within 0.5 % agreement. In our calculations, we used a $6 \times 6 \times 12$ Monkhorst–Pack k -point meshes for the Brillouin-zone integration to ensure the convergence of the results. For uniform sampling of the k -space, note that the k points chosen are inversely proportional to the ratio of the lattice vectors of the supercell. The k points chosen in the current simulation were verified to yield a converged minimum energy value. Similar procedure was followed for GSFE calculations of B19 orthorhombic structure. Ionic relaxation was performed by a conjugate gradient algorithm. The energy cut-off of 360 eV was used for the plane-wave basis set. The total energy was converged to less than 10^{-5} eV per atom. For GSFE calculations, a full internal atom relaxation, including perpendicular and parallel directions to the fault plane, was allowed for minimizing the short-range interaction between misfitted layers in the vicinity of the fault plane. During the relaxation

process, the total energy of the deformed crystal was minimized.

Results

Lattice Constant Calculations

In this section, we demonstrate a general methodology to obtain the lattice constants for the β and α'' crystal structures in detail. We take Ti-6.25Nb-31.25Zr as an example case (note that the compositions used hereafter are all atomic percentage). In order to derive the β lattice constant, the total structural energies of the β supercell are first obtained by varying the lattice parameters. Then the equilibrium lattice constant (a_0) is taken as the one corresponding to the minimum structural energy as shown in Fig. 1. Using this methodology, the equilibrium lattice constant of Ti-6.25Nb-31.25Zr is calculated as 3.35 Å.

Since an orthorhombic (α'') crystal has three different lattice parameters, a , b , and c for the angles $\alpha = \beta = \gamma = 90^\circ$, it is first important to obtain the equilibrium volume. In all the B19 crystals considered, ' a ' is the smallest, ' b ' is the intermediate, and ' c ' is the largest lattice parameter. Figure 2 shows the structural energy variation with respect to different volumes for the case of Ti-6.25Nb-31.25Zr, and the calculated equilibrium volume is 76 Å³. For a constant equilibrium volume, it is now convenient to obtain the structural energy of the crystal by varying only two parameters, a/c and b/c ratios. We note that the ratios, $a/c = 0.59$ and $b/c = 0.92$, correspond to the lowest energy for the case of Ti-6.25Nb-31.25Zr, as shown in potential energy surface of Fig. 3. Hence, the equilibrium lattice constants a , b , and c can be obtained

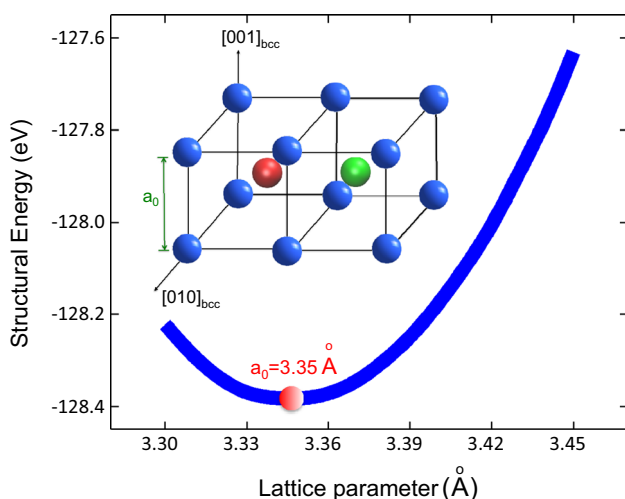


Fig. 1 Structural energy variation with respect to lattice parameters for Ti-6.25Nb-31.25Zr alloy

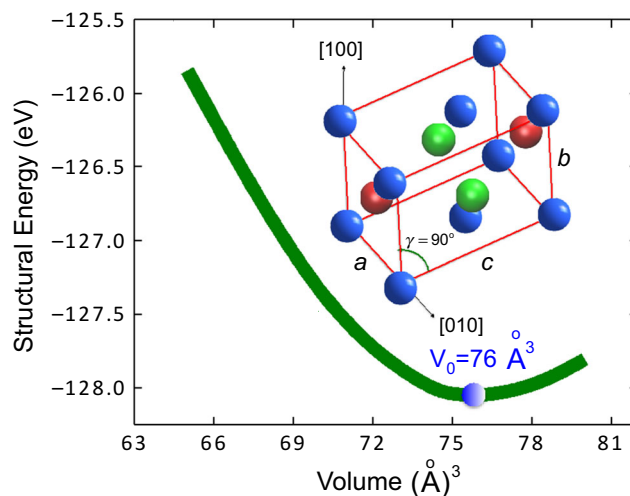


Fig. 2 Structural energy variation with respect to volume change for a B19 Ti-6.25Nb-31.25Zr crystal

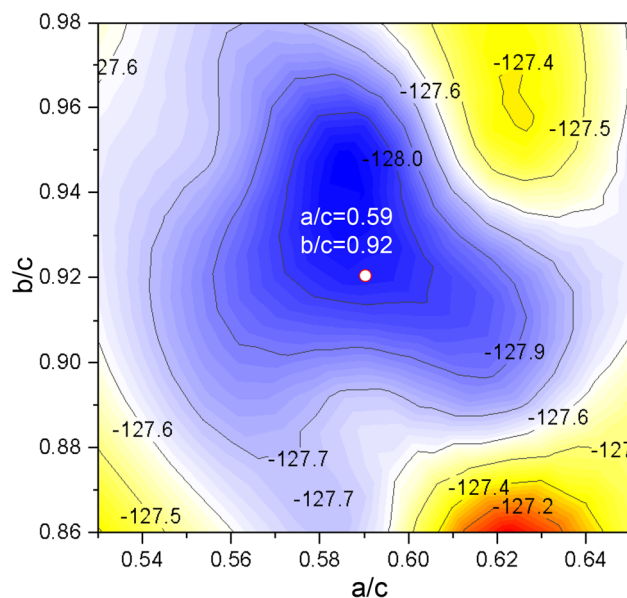


Fig. 3 Energy (in eV) versus a/c and b/c ratios under constant equilibrium volume for a B19 Ti-6.25Nb-31.25Zr crystal

from the knowledge of equilibrium volume and the lattice parameters' ratios. We used similar methodology to calculate the lattice constants for all other alloys considered in the present study. A comprehensive list of lattice parameters for Ti-Nb-Zr and Ti-Nb-Ta alloys for both β and B19 α'' structures is listed in Tables 1 and 2.

To further study the composition dependence of Nb, Zr, and Ta on the β and B19 α'' lattice parameters, we plot the results of Tables 1 and 2 in Figs. 4, 5, and 6. It is important to note that the theoretical values reported in Figs. 4, 5, and 6 are in excellent agreement with the experimentally observed values (within 3 %) [8]. Figure 4 shows that the β

Table 1 Lattice constant (a_0) of β and orthorhombic phases (a , b , c) of Ti–Nb–Zr alloys. The units are in Angstroms

Alloys	Theory (this study)				Experiments			
	a_0	a	b	c	a_0	a	b	c
Ti–12.5Nb	3.26	3.01	4.65	4.95	3.285	3.02	4.661	4.985
Ti–25Nb	3.26	3.17	4.62	4.76	3.285	3.193	4.635	4.797
Ti–6.25Nb–6.25Zr	3.28	3.03	4.79	5.17	–	–	–	–
Ti–25Nb–6.25Zr	3.28	3.24	4.65	4.81	3.30	3.25 ^a	4.66	4.83
Ti–12.5Nb–12.5Zr	3.29	3.08	4.73	5.01	–	3.09 ^b	4.75	5.03
Ti–18.75Nb–12.5Zr	3.29	3.17	4.66	4.89	3.32	3.19 ^c	4.68	4.90
Ti–37.25Nb–12.5Zr	3.29	3.27	4.62	4.85	–	–	–	–
Ti–6.25Nb–18.75Zr	3.31	3.04	4.79	5.18	–	–	–	–
Ti–12.5Nb–25Zr	3.33	3.16	4.76	5.02	3.36	3.18 ^d	4.79	5.03
Ti–18.75Nb–25Zr	3.33	3.18	4.67	4.90	–	–	–	–
Ti–25Nb–25Zr	3.33	3.23	4.65	4.81	–	–	–	–
Ti–6.25Nb–31.25Zr	3.35	3.06	4.80	5.21	3.386	3.09 ^e	4.82	5.22
Ti–12.5Nb–37.5Zr	3.38	3.18	4.77	5.03	–	–	–	–
Ti–37.5Nb–18.75Zr	3.31	3.28	4.63	4.86	–	–	–	–
Ti–12.5Nb–18.75Zr	3.31	3.08	4.70	4.98	–	–	–	–
Ti–18.75Nb	3.26	3.09	4.63	4.87	–	–	–	–
Ti–18.75Nb–6.25Zr	3.28	3.17	4.64	4.87	–	–	–	–

The spaces marked with dash (–) represent unavailable experimental data. Approximate values based on the following compositions [8]

^a Ti–20Nb–6Zr

^b Ti–13Nb–12Zr

^c Ti–16Nb–12Zr

^d Ti–10Nb–24Zr

^e Ti–6Nb–30Zr

Table 2 Lattice constant (a_0) of β and orthorhombic phases (a , b , c) of Ti–Ta–Nb alloys. The units are in Angstroms

Alloys	Theory (this study)				Experiments			
	a_0	a	b	c	a_0	a	b	c
Ti–6.25Nb–6.25Ta	3.26	3.06	4.66	4.93	–	–	–	–
Ti–25Nb–6.25Ta	3.26	3.11	4.66	4.77	–	–	–	–
Ti–12.5Nb–12.5Ta	3.27	3.15	4.65	4.84	–	3.17 ^a	4.65	4.85
Ti–18.75Nb–12.5Ta	3.26	3.19	4.64	4.76	3.28	3.21 ^b	4.64	4.78
Ti–37.25Nb–12.5Ta	3.26	3.25	4.64	4.73	–	–	–	–
Ti–6.25Nb–18.75Ta	3.26	3.15	4.64	4.81	–	3.16 ^c	4.64	4.83
Ti–12.5Nb–25Ta	3.27	3.26	4.65	4.74	–	–	–	–
Ti–18.75Nb–25Ta	3.26	3.27	4.66	4.72	–	–	–	–
Ti–25Nb–25Ta	3.27	3.28	4.66	4.71	–	–	–	–
Ti–6.25Nb–31.25Ta	3.25	3.23	4.63	4.72	3.28	3.26 ^d	4.64	4.73
Ti–12.5Nb–37.5Ta	3.27	3.25	4.66	4.71	–	–	–	–
Ti–37.5Nb–18.75Ta	3.27	3.26	4.67	4.74	–	–	–	–

The spaces marked with dash (–) represent unavailable experimental data. Approximate values based on the following compositions [8]

^a Ti–14Nb–10Ta

^b Ti–17Nb–10Ta

^c Ti–6.25Nb–20Ta

^d Ti–6.25Nb–30Ta

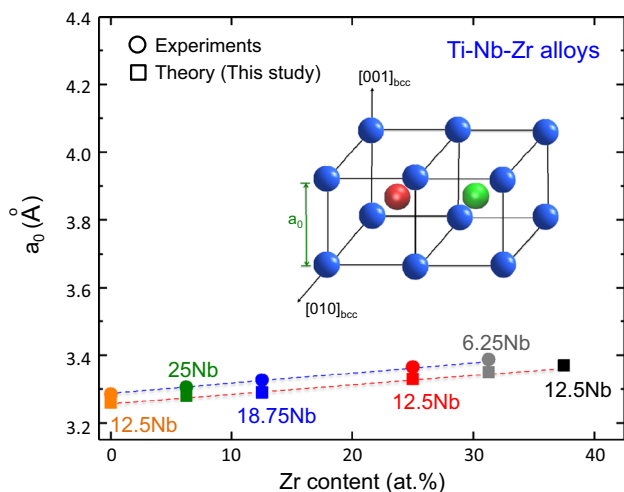


Fig. 4 Lattice constant of Ti–Nb–Zr alloys versus Zr composition. The broken lines are shown to aid the eye

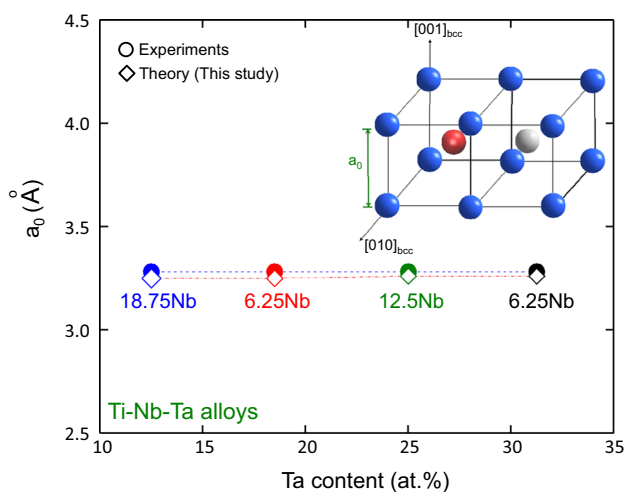


Fig. 5 Lattice constants of Ti–Nb–Ta alloys versus Ta composition. The broken lines are shown to guide the eye

phase lattice constants (a_0) for Ti–Nb–Zr alloys are strongly dependent on the Zr content. An increase in the Zr content linearly increases a_0 , and the relationship between Zr content and a_0 can be expressed as follows:

$$a_0(\text{Zr at.}\%) = 3.2585 + 0.0029 \times C_{\text{Zr(at.}\%)},$$

where C is the concentration of Zr in at.%. On the other hand, in Fig. 5, we observe that both Nb and Ta do not have a considerable effect on a_0 for Ti–Nb–Ta alloys.

In order to investigate the effects of Nb content on the orthorhombic (B19) lattice parameters, we plot a , b , and c as a function of Nb content for some of the alloys listed in Table 1 where experimental data [8] are also available. Interestingly, from Fig. 6, we see that the Nb content affects the B19 lattice constants. In particular, the lattice

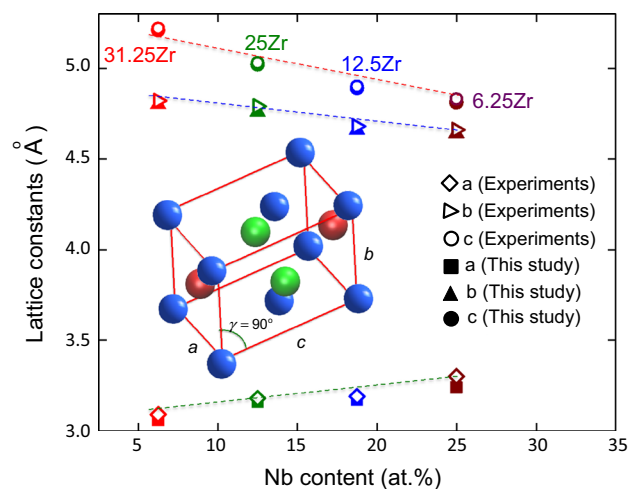


Fig. 6 Lattice constants (a , b , c) of B19 Ti–Nb–Zr alloys versus Nb content

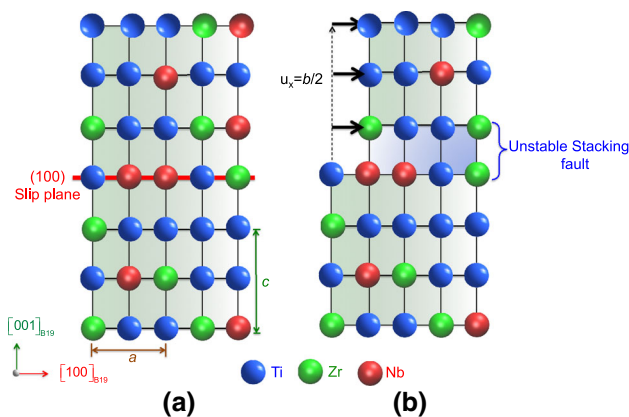


Fig. 7 **a** A perfect B19 lattice as viewed along the $\langle 010 \rangle$ direction. **b** Deformed B19 lattice after shear by half the magnitude of Burgers vector ($u_x = b/2$)

parameter a increases, while b and c decrease with an increase in Nb content regardless of the Zr content in these alloys. These observations are validated both experimentally and theoretically in Fig. 6.

Slip and GSFE Curves in B19 Ti-Based Alloys

An important criterion to maximize reversible strain is to minimize plastic deformation accumulating via dislocation slip in α'' martensite during phase transformation. The possible slip systems in B19 orthorhombic crystal structures include a family of $\{110\}\langle 110 \rangle$ and $\{100\}\langle 100 \rangle$ systems [16, 17]. Consider Fig. 7a where the B19 crystal structure is shown as viewed along the $[0\bar{1}0]$ direction. It is worth pointing out that in Fig. 7a, the slip system $(001)[100]$ corresponds to the largest interplanar distance (axis c) in $[001]$ direction and the shortest Burgers vector

(axis a) in $[100]$ direction. Based on this slip system, the Burgers vector (b) for B19 Ti–6.25Zr–25Nb lattice is equal to 3.24 Å, for example.

The GSFE is obtained by shearing one half (001) plane of the crystal with respect to another half by continuous rigid displacements of $u_x = nb$ along $[100]$ direction, where b is the magnitude of the Burgers vector and n is a parameter ranging from 0 to 1 [18–20]. Similarly, Fig. 7b is the deformed lattice after shear by half a Burgers vector ($u_x = 0.5b$). The GSFE curves for both alloy systems, Ti–Nb–Ta and Ti–Nb–Zr, for four different compositions exhibiting the highest γ_{us} values and the lowest γ_{us} values are shown in Fig. 8. The γ_{us} is the maximum energy barrier required to nucleate a slip, and corresponds to the displacement of $u_x = 0.5b$ on the GSFE curve. The (001)[100] γ_{us} values for each alloy considered in the present analysis are reported in Table 3, and graphically represented in Fig. 8. The GSFE curve also allows us to derive the $\{100\}\langle 100\rangle$ shear modulus using the equation, $G_{\{100\}\langle 100\rangle} = 2\pi \frac{\partial \gamma}{\partial u_x}|_{\max}$. The magnitudes of the shear moduli for Ti–Nb–Zr and Ti–Nb–Ta alloys are also listed in Table 3.

In the present analysis, we determined that the $\{100\}\langle 100\rangle$ are the active slip systems in Ti–Nb–Zr and Ti–Nb–Ta alloys. We also obtained the GSFE curves for $\{110\}\langle 110\rangle$ slip systems using similar methodology discussed above. The $\{110\}\langle 110\rangle$ γ_{us} values for all the alloys considered are approximately 3–5 times higher than those for $\{100\}\langle 100\rangle$ slip systems. For example, the $\{110\}\langle 110\rangle$ γ_{us} for Ti–6.25Zr–6.25Nb, Ti–18.75Zr–37.5Nb, Ti–25Ta–25Nb, and Ti–6.25Ta–6.25Nb alloys were obtained as 922, 2124, 3276, and 1613 mJ m⁻², respectively. These values are significantly higher than the γ_{us} for $\{100\}\langle 100\rangle$ slip

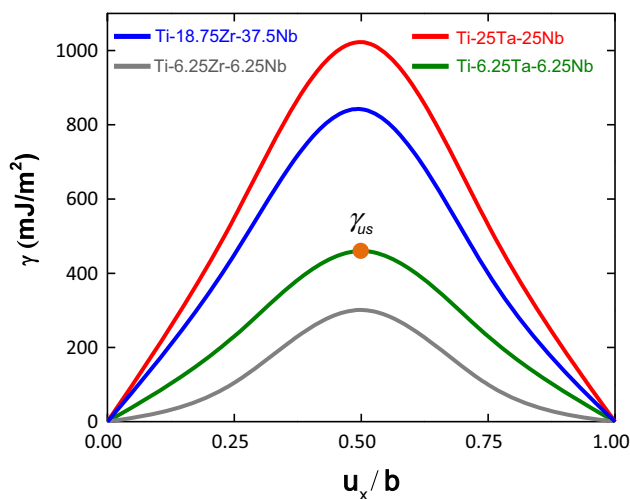


Fig. 8 Generalized stacking fault energy (GSFE) for Ti–Nb–Ta and Ti–Nb–Zr alloys for the compositions exhibiting the highest and the lowest values

systems, and hence rule out the possibility of slip nucleation in $\{110\}\langle 110\rangle$ slip systems. Recently, similar theoretical calculations [21] on NiTiHf have shown that the activation of slip systems of $\{110\}\langle 110\rangle$ family in B19 lattice is unfavorable due to the high energy barrier associated with the generalized stacking fault energy (GSFE) curve, and ultimately high CRSS (in orders of GPa). Hence, the $\{100\}\langle 100\rangle$ slip system is considered for further analysis in the present paper.

Figure 9a, b shows the ternary contour plot of γ_{us} variation for Ti–Nb–Zr and Ti–Nb–Ta alloys. Upon comparing the plots, we observe that the γ_{us} values for all Ti–Nb–Ta alloys are higher than that of Ti–Nb–Zr alloys for the same composition of Ti and Nb. For the case of Ti–Nb–Zr alloys, the maximum γ_{us} values lie in the region of high Nb and high Zr content, shown by as shown by red shades in Fig. 9a, while in the case of Ti–Nb–Ta alloys, the maximum γ_{us} values are obtained in low Nb and high Ta content. The lower γ_{us} values for Ti–Nb–Zr lie along the constant Nb content of 12.5 at.%, while for Ti–Nb–Ta alloys, the region is observed in low Ta and low Nb content. As we see later, the magnitude of γ_{us} influences the CRSS for martensite slip nucleation. Therefore, the results in Fig. 9 provide useful insights for slip resistance associated with different compositions of Nb, Ta, and Zr in Ti-based alloys.

Peierls Nabarro Modeling of the Critical Resolved Shear Stress (CRSS) for Slip

The modified PN formalism is adopted in the current work to calculate the slip stress, which is an advancement to the original PN model [22, 23]. The major advancements of the modified PN formalism are the use of actual energy landscape (GSFE) of the alloy to calculate the energy variation with respect to the dislocation position and the consideration of the lattice discreteness to obtain the misfit energy curve [24–27]. The misfit energy across a slip plane is defined as the sum over energy contributions due to slip between pairs of atomic planes [26, 27], and can be obtained from the GSFE as follows:

$$E_{\gamma}^s = \int_{-\infty}^{+\infty} \gamma_{\text{GSFE}}(f(x)) dx \quad (1)$$

The term γ_{GSFE} is the GSFE energy landscape (as shown in Fig. 8) expressed in sinusoidal form, and $f(x)$ is defined as the disregistry function which is a measure of the slip distribution on the slip plane, $u_A - u_B$ as shown in Fig. 10a. The solution to $f(x)$ can be written as follows [26, 27]:

Table 3 The γ_{us} values, the shear moduli, and the CRSS for slip nucleation in B19 Ti–Nb–Zr and Ti–Nb–Ta alloys

Ti–Nb–Zr Alloys (at.%)	γ_{us} (mJ m^{-2})	Shear modulus (in GPa) $G_{\{100\}\{100\}}$	CRSS, $\tau_{\text{critical}}^{\text{slip}}$ (MPa)	Ti–Nb–Ta Alloys (at.%)	γ_{us} (mJ m^{-2})	Shear modulus (in GPa) $G_{\{100\}\{100\}}$	CRSS, $\tau_{\text{critical}}^{\text{slip}}$ (MPa)
Ti–6.25Nb–6.25Zr	301	11	82	Ti–6.25Nb–6.25Ta	460	16	127
Ti–6.25Nb–18.75Zr	315	12	88	Ti–6.25Nb–18.75Ta	550	20	152
Ti–6.25Nb–25Zr	386	14	109	Ti–6.25Nb–25Ta	901	32	244
Ti–6.25Nb–31.25Zr	475	17	132	Ti–6.25Nb–31.25Ta	912	32	250
Ti–12.5Nb	532	18	144	Ti–12.5Nb–6.25Ta	810	29	224
Ti–12.5Nb–6.25Zr	387	13	110	Ti–12.5Nb–12.5Ta	953	34	263
Ti–12.5Nb–12.5Zr	311	11	86	Ti–12.5Nb–18.75Ta	997	35	271
Ti–12.5Nb–18.75Zr	381	14	101	Ti–12.5Nb–25Ta	1006	36	278
Ti–12.5Nb–25Zr	410	24	125	Ti–12.5Nb–37.5Ta	1013	36	280
Ti–12.5Nb–37.5Zr	678	26	184	Ti–18.75Nb–6.25Ta	805	29	222
Ti–18.75Nb–12.5Zr	752	27	190	Ti–18.75Nb–12.5Ta	920	33	254
Ti–18.75Nb–25Zr	760	27	200	Ti–18.75Nb–18.75Ta	922	33	255
Ti–25Nb	843	29	228	Ti–18.75Nb–25Ta	923	33	255
Ti–25Nb–6.25Zr	754	26	195	Ti–25Nb–6.25Ta	857	31	237
Ti–25Nb–12.5Zr	756	27	196	Ti–25Nb–12.5Ta	950	34	261
Ti–25Nb–25Zr	787	28	206	Ti–25Nb–18.75Ta	1011	36	280
Ti–37.5Nb	852	31	231	Ti–25Nb–25Ta	1023	37	283
Ti–37.5Nb–6.25Zr	827	30	222	Ti–31.25Nb–25Ta	847	30	234
Ti–37.5Nb–12.5Zr	831	29	225	Ti–37.5Nb–12.5Ta	936	32	259
Ti–37.5Nb–18.75Zr	842	30	227	Ti–37.5Nb–18.75Ta	957	33	264
Ti–50Nb	855	31	232				
Ti–18.75Nb	755	26	196				
Ti–18.75Nb–6.25Zr	679	24	183				
Ti–18.75Nb–31.25Zr	788	28	207				

$$f(x) = \frac{b}{\pi} \left(\tan^{-1} \left(\frac{x}{\xi} \right) \right) + \frac{b}{2}, \quad (2)$$

where b is the magnitude of the Burgers vector of the slip

dislocation, x is the position of the dislocation line, and ξ is the half-core width of the dislocation given by $d/(2(1 - \nu))$ [26], where d is the $\{001\}$ interplanar distance, and ν is the Poisson ratio. The discrete form of Eq. (1) can be written as

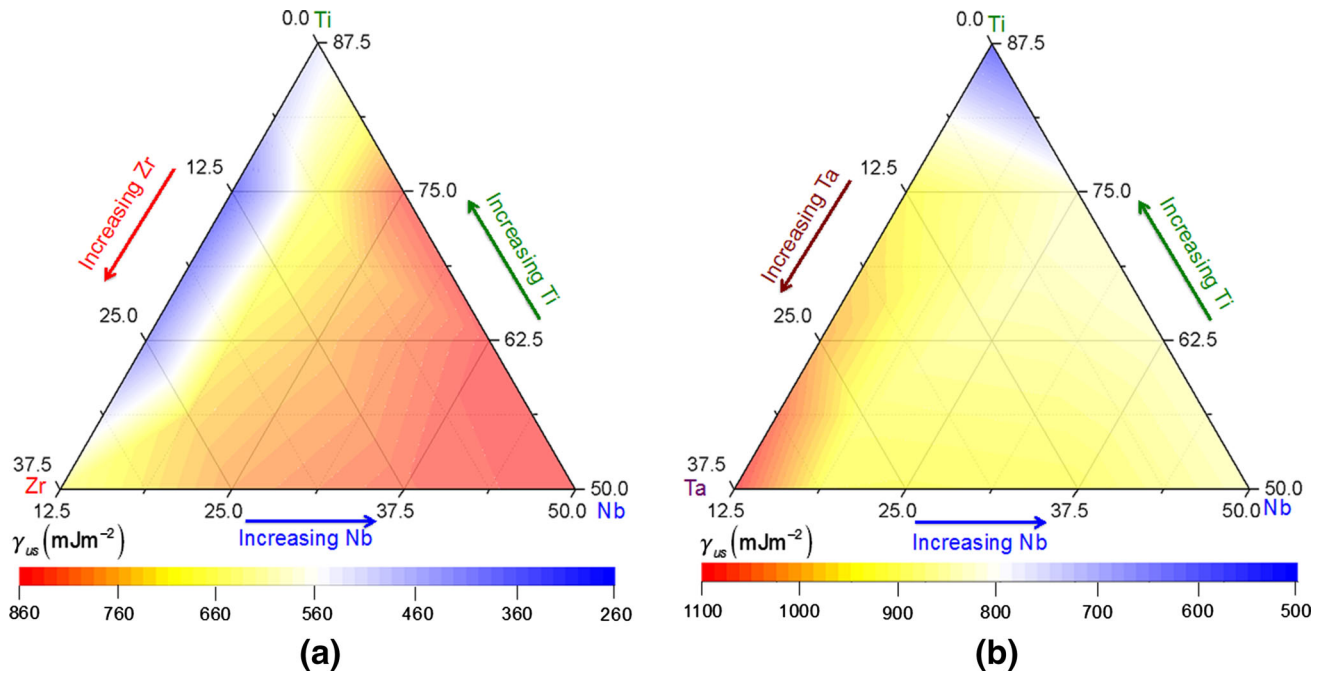
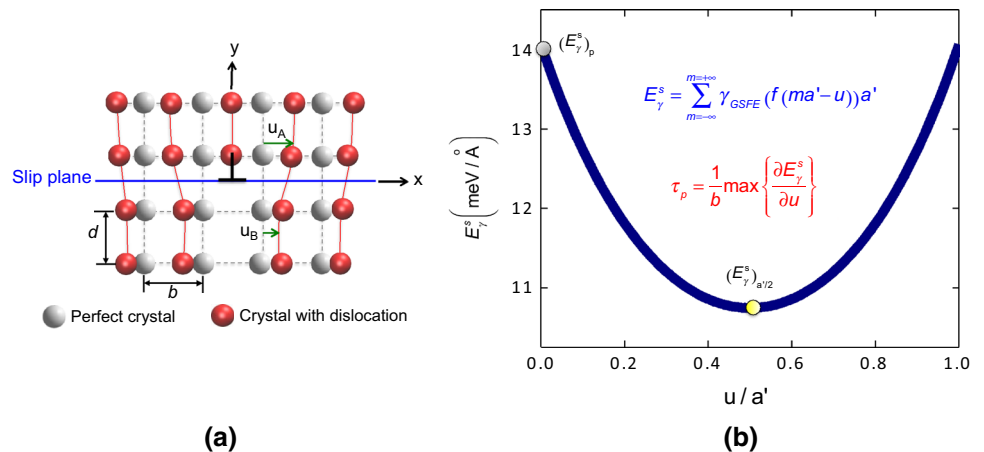


Fig. 9 Composition dependence of unstable fault energy in **a** Ti–Nb–Zr, **b** Ti–Nb–Ta alloys

Fig. 10 a Schematic of the PN model for slip nucleation. **b** Misfit energy (E_γ^s) variation with respect to the dislocation position for the case of Ti–6.25Nb–25Ta



$$E_\gamma^s = \sum_{m=-\infty}^{m=+\infty} \gamma_{\text{GSFE}}(f(ma' - u))a', \quad (3)$$

where m is an integer, u is the position of the dislocation line, and a' is the lattice periodicity defined as the shortest distance between two equivalent atomic rows in the direction of the dislocation displacement. The numerical solution to Eq. (3) for the case of Ti–6.25Nb–25Ta is shown in Fig. 10b. In Fig. 10b, the term $(E_\gamma^s)_{a/2}$ is the minimum of the E_γ^s function and provides an estimate of the core energy of the dislocation. Similarly, the term $(E_\gamma^s)_p$ is the Peierls energy (marked on Fig. 10b) which is

the amplitude of the variation and the barrier required to move the dislocation. The Peierls stress is calculated as the maximum slope of the misfit energy curve which describes the potential energy of the dislocation as a function of the dislocation position u [26], and can be written as follows:

$$\tau_{\text{critical}}^{\text{slip}} = \max \left\{ \frac{1}{b} \left(\frac{\partial E_\gamma^s}{\partial u} \right) \right\} \quad (4)$$

The values of the CRSS for slip using Eq. (4) are given in Table 3. We note that the γ_{us} and ultimately the slip stress of Ti–Nb–Ta alloys are higher than Ti–Nb–Zr alloys for the same composition of Ti and Nb. Therefore, higher the γ_{us} , the higher is the CRSS obtained using Eq. (4).

Discussion and Implications of Results

Figure 11 shows the magnitudes of the CRSS for martensite slip in Ti–Nb–Zr alloys for several compositions of Nb and Zr. The results for the binary Ti–Nb are also included. Two important observations are noted in the plot: (i) First, with an increase in Nb content, the CRSS for slip increases. The net increase in CRSS upon increasing Nb content from 6.25 to 12.5 at.% for a constant Zr content is within 40 MPa, while a dramatic increase in the stress (approximately 60 %) is observed upon increasing Nb content from 12.5 to 18.75 at.%. (ii) Secondly, the results show that a critical Zr content exists for each Nb content beyond which the magnitude of CRSS for slip increases with an increase in Zr content. For 6.25, 12.5, 18.75, 25, and 37.5 at.% Nb contents, the slip stress increases linearly with an increase in Zr content beyond 12.5, 12.5, 6.25, 6.25, and 6.25 at.%, respectively.

We note that Ti–24Zr–13Nb does not exhibit superelasticity, as validated by experiments [8], and the reason behind this may be due a low CRSS for slip compared to the martensite transformation stress. For example, the calculated CRSS of Ti–25Zr–12.5Nb in the present analysis, which has a similar composition to Ti–24Zr–13Nb, is 125 MPa. In such a case, it is easier to deform by slip than to induce martensite transformation, and this accumulates the permanent irreversible strain. On the other hand, for the case of Ti–25Nb, it is experimentally observed that the transformation strain of approximately 2.2 % is fully recovered [8]. This can be a result of the high CRSS for slip nucleation. Theoretically, we obtained the CRSS of 228 MPa for the case of Ti–25Nb, a 113 % increase in the CRSS compared to Ti–12.5Nb–25Zr where no

pseudoelasticity was observed. Hence, from the present analysis, the magnitude of the CRSS can be related to the recoverability of Ti–Nb-based alloys to a first approximation. In other words, the higher slip resistance favors martensite transformation, thereby inhibiting nucleation and accumulation of martensite slip. Nonetheless, the difference in the CRSS for slip and the martensite transformation stress is another important factor to consider.

Similarly, Fig. 12 shows the effect of Nb and Ta contents on the CRSS for Ti–Nb–Ta alloys. Here, we point to the major difference between the role of Ta compared to Zr on the CRSS for slip. We observe that the addition of Ta content on binary Ti–Nb alloys increases the CRSS for slip. For example, the CRSS for slip for Ti–12.5Nb is 144 MPa while that of Ti–12.5Nb–12.5Ta is 263 MPa, an increase in the slip stress by more than 80 % with 12.5 at.% Ta addition. While for the same composition of Ti and Nb, the slip stress for Ti–12.5Nb–12.5Zr is 86 MPa, a decrease in the slip stress by 25 %. The initial decrease (or increase) of the slip stress upon alloying with Zr (or Ta) has been reported previously in experiments [9, 10, 12]. The slip stress for binary Ti–22Nb is 370 MPa while that of Ti–22Nb–6Zr and Ti–22Nb–6Ta are approximately 310 and 440 MPa, respectively. It is important to note that the stresses reported experimentally are based on 0.2 % strain offset, and do not correspond to the CRSS for slip. If we assume that the Schmid factor of the activated slip system is 0.5, the CRSS for Ti–22Nb is 185 MPa from experimental measurements. Overall, if we compare the magnitudes of the CRSS in Ti–Nb–Ta alloys compared to Ti–Nb–Zr for the same composition of Ti and Nb, we conclude that Ta is more effective in increasing martensite slip resistance than Zr.

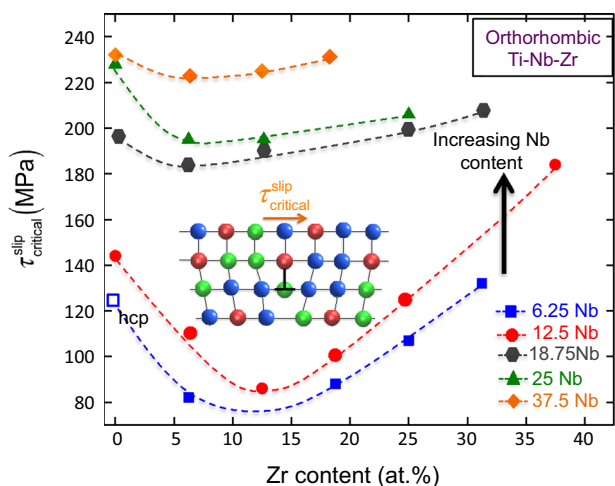


Fig. 11 CRSS for martensite slip nucleation as a function of Zr content in Ti–Nb–Zr alloys. The CRSS for hcp Ti–6.25Nb martensite nucleation is also shown (as *open square*)

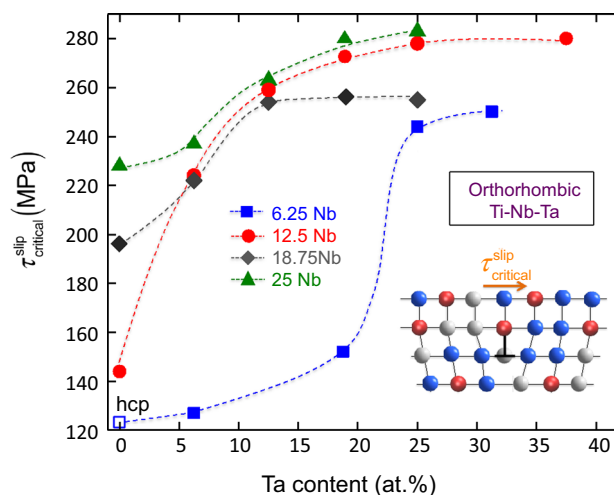


Fig. 12 CRSS for martensite slip nucleation as a function of Ta content in Ti–Nb–Ta alloys. The CRSS for hcp Ti–6.25Nb martensite nucleation is also shown (as *open square*)

In the present work, we also calculated the maximum transformation strains based on the Lattice Deformation Theory (LDT) [28, 29] as shown in Figs. 13, 14, and 15. The details of the LDT are provided in “Appendix” section. In Fig. 13, we show the orientation dependence of the transformation strains for Ti–6.25Nb–6.25Zr and Ti–6.25Nb–6.25Ta alloys. Note that two alloy compositions reported in Fig. 13 exhibit the highest transformation strains compared to all other alloys under consideration. It is worth pointing out that in all the alloy systems, the maximum transformation strain is observed in the [110] orientation, as in the case for Ti–6.25Nb–6.25Zr and Ti–6.25Nb–6.25Ta (Fig. 13). The maximum transformation strain for Ti–6.25Nb–6.25Zr is 11 % which is higher than that of Ti–6.25Nb–6.25Ta by 5 %. Upon comparing the maximum transformation strains in Figs. 13, 14, and 15, we conclude that Zr is a better alloying element compared to Ta for increasing the transformation strain.

We calculated the transformation strains for most of the alloy systems listed in Tables 2 and 3, and the maximum transformation strains are plotted in Figs. 14 and 15. From these plots, we observe that increasing Nb content in both Ti–Nb–Ta and Ti–Nb–Zr alloys for the same Zr or Ta content decreases the maximum transformation strain. This is in agreement with the experimental observations [10] for binary Ti–Nb alloys where a decrease in transformation strain is seen with an increase in Nb content. It was found that an increase in Nb content from 15 to 25 at.% decreases the transformation strain by 45 % (4.5–2.5 %). Interestingly, we observe that increase in Zr content increases the maximum transformation strain initially, but beyond a critical Zr content, the transformation strain starts to decrease. The critical Zr content is found to be 12.5 at.% for all the alloys considered. On the other hand, no such critical Ta content exists for Ti–Nb–Ta alloys. Moreover, the maximum transformation strains of Ti–Nb–Ta alloys

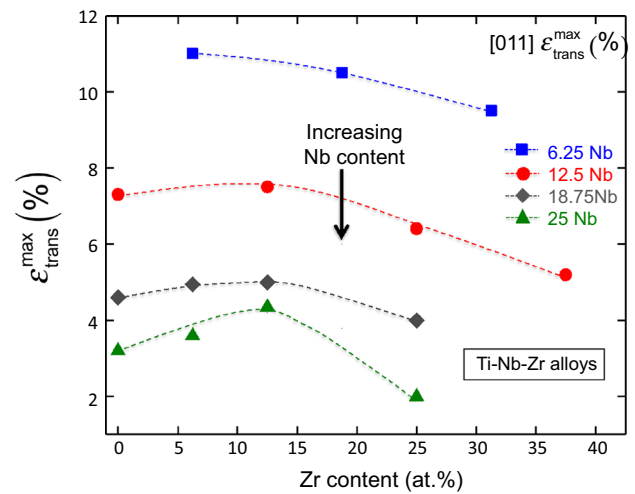


Fig. 14 The maximum [011] transformation strain (tension) as a function of Zr content in Ti–Nb–Zr alloys

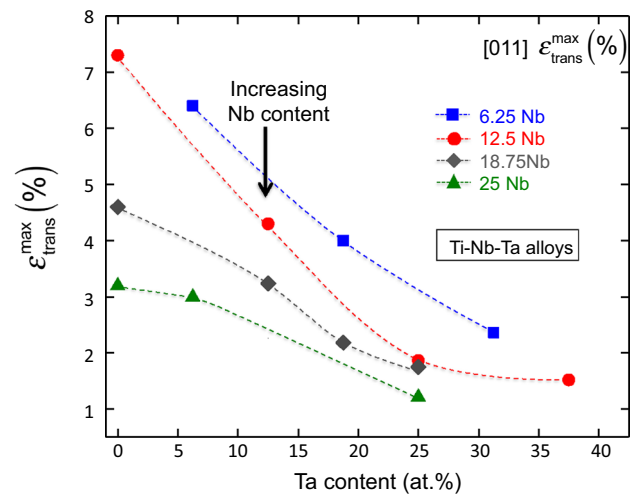
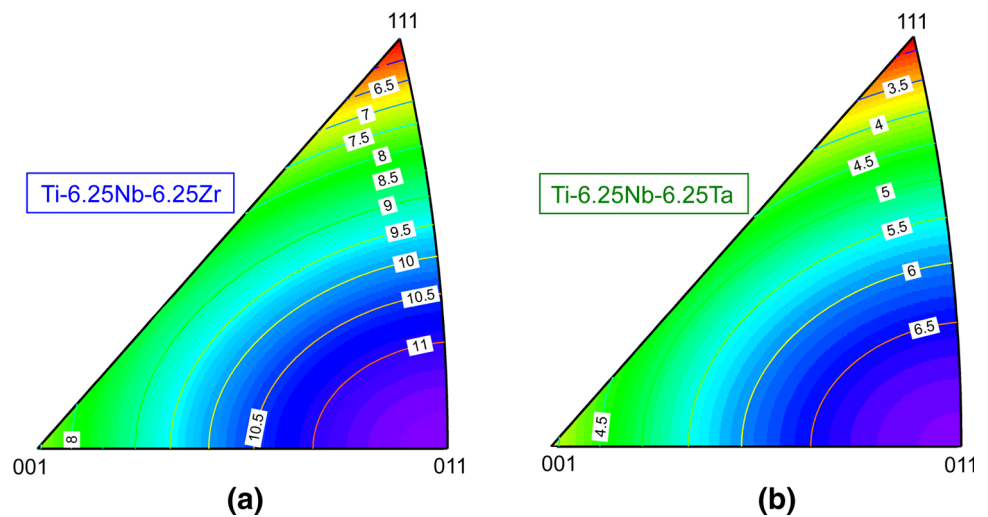


Fig. 15 The maximum [011] transformation strain (tension) as a function of Ta content in Ti–Nb–Zr alloys

Fig. 13 Orientation dependence of the transformation strain (tension) based on lattice deformation theory in **a** Ti–6.25Nb–6.25Zr and **b** Ti–6.25Nb–6.25Ta alloys



are lower than those of Ti–Nb–Zr alloys for the same composition of Ti and Nb.

We showed that the CRSS for slip is dictated by the unstable energy barrier of the GSFE curve using PN formalism. The higher the γ_{us} value, the higher is the slip nucleation stress. Figure 16 shows that the CRSS for martensite slip nucleation in both Ti–Nb–Ta and Ti–Nb–Zr alloys shows a linear dependence on the unstable stacking fault energy value (γ_{us}). This linear dependence can be expressed by the following equation:

$$\tau_{critical}^{slip}(\gamma_{us}) = 0.272 \times \gamma_{us} \quad (5)$$

It is important to point out that the transformation strain scales approximately with c/a_0 ratio in Ti–Nb alloys based on our calculations. We also showed that Ta and Zr do not exhibit similar effect on the CRSS and the transformation strains. Specially, we reveal a nonlinear dependence of the CRSS and the transformation strains on the Ta, Nb, and Zr contents. The critical compositions of Zr and Ta have been determined beyond which the martensite slip stress or the maximum transformation strains change (either increase or decrease). It is worth emphasizing that the CRSS values for slip obtained in the present analysis are at 0 K, while experimental values are reported at finite temperatures. The reason for higher CRSS values obtained theoretically in the present case compared to the experimental values may be due to the temperature dependence of the elastic modulus of martensite. Experiment [30] has shown that a decrease in temperature (below M_s) increases the martensite elastic modulus in Ti-based shape memory alloy, and therefore, Eq. (4) yields high CRSS at 0 K compared to the experimentally obtained CRSS values at finite temperatures. In summary, we considered the CRSS and the transformation

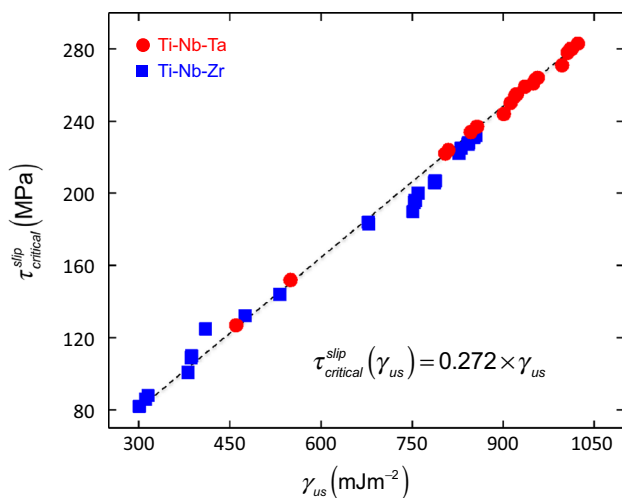


Fig. 16 The dependence of the CRSS for martensite slip nucleation ($\tau_{critical}^{slip}$) on the unstable stacking fault energy values (γ_{us}) for Ti–Nb–Ta and Ti–Nb–Zr alloys. The dashed line represents the best fit to data given by the equation in the inset

strains for a large number of Ti–Nb–Ta and Ti–Nb–Zr alloys (over 40 cases) with wide composition range of Ta, Zr, and Nb. This is a major contribution to future alloy design via composition optimization.

Conclusions

In summary, we draw the following conclusion from the current paper:

1. Using modified PN formalism incorporating the generalized stacking fault energy (GSFE) from DFT calculations, we predict the martensite slip resistance in Ti–Nb–Ta and Ti–Nb–Zr alloys over wide composition of Nb, Ta, and Zr. The CRSS levels are in the range 80–280 MPa. We propose a simple linear relation between the CRSS and unstable fault energy.
2. We calculate the lattice constants of Ti–Ta–Nb and Ti–Nb–Zr for β and α' B19 orthorhombic structures noting that the superelasticity in these alloys is attributed to the thermoelastic transformation between the two phases. We compare our theoretically obtained values with the available experimental data showing excellent agreement.
3. Using lattice deformation theory (LDT), we calculate the maximum transformation strains in both Ti–Nb–Ta and Ti–Nb–Zr alloys. We show that the maximum transformation strain is higher in the case of Ti–Nb–Zr alloys compared to Ti–Nb–Ta alloys for the same composition of Ti and Nb. The strains exceed to 10 % in some cases.
4. We show that the addition of Zr increases the transformation strain up to a critical Zr content beyond which the transformation strain starts to decrease. The maximum transformation strain is observed in the [011] orientation for all the alloys considered in the present analysis. Large additions of Ta and Nb decreases the maximum transformation strain in the alloys from 11 % to as low as 1.5 %.
5. From the present analysis, Ta is considered more effective in Ti–Nb alloys in increasing the CRSS compared to Zr, while Zr is more effective in increasing the transformation strain compared to Ta.

Acknowledgments The support from Nyquist Chair Fund and partial support from National Science Foundation grant NSF CMMI-1333884 are gratefully acknowledged. We thank Mr. George Li for providing assistance with the LDT simulations setup.

Appendix

The Lattice Deformation Theory (LDT) [29] estimates the recoverable transformation strains by directly considering the 6 lattice correspondences between the bcc austenite and

the orthorhombic martensite crystal structures. For each lattice correspondence variant, a symmetric transformation matrix \mathbf{U} can be determined. The components of \mathbf{U} matrix are functions of the lattice constants of the parent austenite and transformed martensite phases. An example of \mathbf{U} for the case of cubic to orthorhombic transformation is

$$\mathbf{U}_1 = \begin{bmatrix} \alpha & 0 & 0 \\ 0 & \frac{\gamma + \beta}{2} & \frac{\gamma - \beta}{2} \\ 0 & \frac{\gamma - \beta}{2} & \frac{\gamma + \beta}{2} \end{bmatrix}, \quad (6)$$

where $\alpha = \sqrt{2}a/a_0$, $\beta = b/a_0$, $\gamma = \sqrt{2}c/a_0$, a_0 , and a , b , and c are the lattice constants of the bcc austenite and the orthorhombic martensite phases, respectively.

The maximum recoverable strains is obtained as

$$\varepsilon = \sqrt{\vec{e} \cdot (\mathbf{F}^T \mathbf{F}) \vec{e}} - 1, \quad (7)$$

where \mathbf{F} is the deformation gradient and \vec{e} is the unit vector in the crystallographic direction of interest. Using polar decomposition theorem, the deformation gradient \mathbf{F} can be written as

$$\mathbf{F} = \mathbf{R}\mathbf{U}, \quad (8)$$

where \mathbf{R} represents a rigid body rotation and \mathbf{U} is the symmetric part of \mathbf{F} .

Upon substituting Eq. (8) into Eq. (7), we have the following equivalent equation:

$$\varepsilon = \sqrt{\vec{e} \cdot (\mathbf{U}^T \mathbf{R}^T \mathbf{R} \mathbf{U}) \vec{e}} - 1 = \sqrt{\vec{e} \cdot (\mathbf{U}^T \mathbf{U}) \vec{e}} - 1 \quad (9)$$

References

- Baker C (1971) Shape memory behavior in Ti–35 wt% Nb alloy. *J Met Sci* 5:92–100
- Duerig TW, Albrecht J, Richter D, Fischer P (1982) Formation and reversion of stress induced martensite in Ti–10 V–2Fe–3Al. *Acta Metall* 30:2161–2172
- Duerig TW, Richter DF, Albrecht J (1982) Shape memory in Ti–10 V–2Fe–3Al. *Scr Metall* 16:957–961
- Blackburn MJ, Feeney JA (1970) Stress-induced transformations in Ti–Mo alloys. DTIC Document
- Hochstuhl P, Obst B (1982) Beta-phase instability and martensitic transformation in Ti–22 at% Nb alloy. *Le Journal de Physique Colloques* 43:C4-133–C4-138
- Ozaki T, Matsumoto H, Watanabe S, Hanada S (2004) Beta Ti alloys with low Young's modulus. *Mater Trans* 45:2776–2779
- Hao YL, Li SJ, Sun SY, Zheng CY, Hu QM, Yang R (2005) Super-elastic titanium alloy with unstable plastic deformation. *Appl Phys Lett* 87:091906
- Kim HY, Fu J, Tobe H, Kim JI, Miyazaki S (2015) Crystal structure, transformation strain, and superelastic property of Ti–Nb–Zr and Ti–Nb–Ta alloys. *Shape Mem Superelast* 1:107–116
- Kim HY, Hashimoto S, Kim JI, Inamura T, Hosoda H, Miyazaki S (2006) Effect of Ta addition on shape memory behavior of Ti–22Nb alloy. *Mater Sci Eng A* 417:120–128
- Kim HY, Ikehara Y, Kim JI, Hosoda H, Miyazaki S (2006) Martensitic transformation, shape memory effect and superelasticity of Ti–Nb binary alloys. *Acta Mater* 54:2419–2429
- Miyazaki S, Kim HY, Hosoda H (2006) Development and characterization of Ni-free Ti-base shape memory and superelastic alloys. *Mater Sci Eng A* 438:18–24
- Kim JI, Kim HY, Inamura T, Hosoda H, Miyazaki S (2005) Shape memory characteristics of Ti–22Nb–(2–8) Zr (at.%) biomedical alloys. *Mater Sci Eng A* 403:334–339
- Karaman I, Sehitoglu H, Beaudoin AJ, Chumlyakov YI, Maier HJ, Tome CN (2000) Modeling the deformation behavior of Hadfield steel single and polycrystals due to twinning and slip. *Acta Mater* 48:2031–2047
- Kresse G, Furthmüller J (1996) Efficient iterative schemes for ab initio total-energy calculations using a plane-wave basis set. *Phys Rev B* 54:11169–11186
- Kresse G, Hafner J (1993) Ab initio molecular dynamics for open-shell transition metals. *Phys Rev B* 48:13115–13118
- Banerjee D, Rowe RG, Hall EL (1990) Deformation of the orthorhombic phase in Ti–Al–Nb alloys. *MRS Proceedings*. Cambridge University Press, Cambridge, p 285
- Poirier J-P (1975) On the slip systems of olivine. *J Geophys Res* 80:4059–4061
- Vitek V (1968) Intrinsic stacking faults in body-centred cubic crystals. *Philos Mag* 18:773–786
- Ojha A, Sehitoglu H (2014) Twinning stress prediction in bcc metals and alloys. *Philos Mag Lett* 94:647–657
- Ojha A, Sehitoglu H, Patriarca L, Maier HJ (2014) Twin nucleation in Fe-based bcc alloys—modeling and experiments. *Modell Simul Mater Sci Eng* 22:075010
- Wang J, Sehitoglu H (2014) Modelling of martensite slip and twinning in NiTiHf shape memory alloys. *Phil Mag* 94:2297–2317
- Lu G, Kioussis N, Bulatov VV, Kaxiras E (2000) The Peierls–Nabarro model revisited. *Philos Mag Lett* 80:675–682
- Peierls R (1940) The size of a dislocation. *Proc Phys Soc* 52:34
- Carrez P, Ferré D, Cordier P (2007) Peierls–Nabarro model for dislocations in MgSiO₃ post-perovskite calculated at 120 GPa from first principles. *Philos Mag* 87:3229–3247
- Joos B, Duesbery MS (1997) The Peierls stress of dislocations: an analytic formula. *Phys Rev Lett* 78:266
- Joós B, Ren Q, Duesbery MS (1994) Peierls–Nabarro model of dislocations in silicon with generalized stacking-fault restoring forces. *Phys Rev B* 50:5890–5898
- Schoeck G (2011) The Peierls stress in a simple cubic lattice. *Phys Status Solidi (b)* 248:2284–2289
- Bhattacharya K (2003) *Microstructure of martensite: why it forms and how it gives rise to the shape-memory effect*. Oxford University Press, Oxford
- Saburi T, Nenno S (1981) The shape memory effect and related phenomena. Solid to solid phase transformations. The Metallurgical Society of AIME, New York, pp 1455–1479
- Inamura T, Hosoda H, Wakashima K, Miyazaki S (2005) Anisotropy and temperature dependence of Young's modulus in textured TiNbAl biomedical shape memory alloy. *Mater Trans* 46:1597–1603